



Investigation of the local catalyst distribution in an aged direct methanol fuel cell MEA by means of differential synchrotron X-ray absorption edge imaging with high energy resolution

Tobias Arlt ^{a,*}, Ingo Manke ^a, Klaus Wippermann ^b, Heinrich Riesemeier ^c, Jürgen Mergel ^b, John Banhart ^a

^a Helmholtz-Zentrum Berlin GmbH, Institute of Applied Materials, Hahn-Meitner-Platz 1, 14109 Berlin, Germany

^b Forschungszentrum Jülich GmbH, Institute of Energy and Climate Research, IEK-3: Fuel Cells, 52425 Jülich, Germany

^c BAM, Bundesanstalt für Materialforschung und -prüfung, Unter den Eichen 87, 12205 Berlin, Germany

HIGHLIGHTS

- Catalyst aging was studied using a novel element selective method.
- Differential synchrotron X-ray radiography revealed ruthenium and platinum distribution quantitatively.
- Upon aging significant redistribution of the catalytic elements in the MEAs of DMFCs were found.
- Differences in XAS characteristics were found between thin and thick catalyst layers.

ARTICLE INFO

Article history:

Received 17 February 2012

Received in revised form

2 August 2012

Accepted 8 August 2012

Available online 21 August 2012

Keywords:

XAS

X-ray energy edge

Membrane electrode assembly

Direct methanol fuel cell

Aging mechanism

X-ray synchrotron radiography

ABSTRACT

Synchrotron X-ray absorption edge imaging with high energy resolution was applied to study aging of fuel cell catalyst materials. The combination of an imaging and a high X-ray energy resolution set-up allows acquiring spatially resolved XAS (XANES and EXAFS) spectra. We analyzed the two-dimensional distribution of Pt and Ru in fresh and aged fuel cell catalysts. Spatially resolved XAS images were taken at the Ru_K edge and at the Pt_{L3} edge. Taking radiographs above and below the absorption edges provides quantitative information about the thickness of the catalytic materials and additional chemical information. A strong influence of the flow field channels and the structure of the gas diffusion layers on the thicknesses of the catalytic elements were found: a thinner catalyst layer was found below the ribs of the flow field geometries as well as under crossing points of fiber bundles of the woven gas diffusion layers.

Crown Copyright © 2012 Published by Elsevier B.V. All rights reserved.

1. Introduction

Direct methanol fuel cells (DMFCs) are very efficient and environmentally friendly energy converters that utilize a fuel with high energy density and therefore demand little or no extra burden on the fuel supply side. The existing energy storage solutions as well as the transport logistics can easily be adapted to this new technique. DMFC applications comprise small portable, stationary and even mobile systems. However, there are durability and performance issues that must be resolved to ensure successful commercialization.

Generally, non-uniform distribution of fluids causes a local and time-dependent inhomogeneity of current distribution, which does not only decrease the DMFC performance but may lead to enhanced degradation. In previous studies, non-uniform distributions of methanol and oxygen have been observed [1–3]. It is well known that a local blockage of oxygen supply is caused by an accumulation and discontinuous removal of product water droplets from the cathode channels [3]. These non-uniform fluid distributions and locally prevented fluid transport processes are assumed to accelerate the aging of the cell components, especially the degradation of catalyst layers. To provide a long-term stable cell operation, detailed knowledge about the underlying aging mechanisms and their correlation to fluid transport [4–8] is essential.

Typical aging processes of DMFCs are Ru dissolution [9] and Ru transfer from the anode to the cathode through the polymer

* Corresponding author. Tel.: +49 30 8062 42822; fax: +49 30 8062 43059.

E-mail address: tobias.arlt@helmholtz-berlin.de (T. Arlt).

membrane [10,11]. Whereas Ru dissolution reduces the activity of the anode catalyst [12], Ru transfer causes a decrease of the oxygen reduction reaction rate at the cathode, which is due to an enhanced reaction rate of transferred methanol on the cathode catalyst [9]. According to Rolison et al., most of the Ru in the PtRu catalyst at the anode is oxidized, whereas only 25% of Ru is alloyed with Pt [13]. Even though a large amount of oxidized Ru is reduced under DMFC operating conditions, a residue of Ru oxide remains in the anode catalyst [14]. The presence of oxidized Ru has an ambivalent effect: on the one hand, oxidized Ru is known to activate the methanol oxidation reaction [15]. On the other hand, oxidized Ru is more susceptible to corrosion [9,14]. Dixon et al. [14] has shown that the reduction of the oxide phase creates unalloyed Ru, which is assumed to be more prone to dissolution and migration to the cathode side compared to the alloyed Ru. XAS and EDX measurements revealed the presence of oxidized Ru in the DMFC cathode and Ru precipitates in the membrane.

In this work, we present a synchrotron X-ray imaging technique [16–23] that enables mapping of the distribution of the catalyst materials platinum (Pt) and ruthenium (Ru) quantitatively and that also provides chemical information via the near edge X-ray absorption fine structure (NEXAFS/XANES) with high two-dimensional spatial resolutions of $\approx 2.1 \mu\text{m}$ [24,25]. The catalyst distribution in fresh and aged DMFC MEAs are compared. Our approach differs from previous studies (e.g. Arlt et al. [26]) where X-ray beams with comparable broad spectral widths around a few 100 eV have been used. This allows only to image the location of catalytic elements within the specimen, but not to quantify its amount. Due to the improved energy resolution applied for the measurements presented in this paper a quantitative analysis of the thickness of the catalysts was possible. Furthermore also chemical information could be obtained with this technique. We should note, that the attenuation contrast imaging set-up presented in Ref. [27] also uses only a broad energy resolution comparable to that in Ref. [26].

2. Experimental setup

The tomography station at the electron storage ring BESSY II at Helmholtz-Zentrum Berlin, Germany, was used for the measurements presented [28]. The tomography station is located at the BAMline which provides a wide energy range of synchrotron radiation between 5 and 70 keV. For radiographic investigations, a W–Si double-crystal monochromator with a high energy resolution of $dE/E \approx 10^{-4}$ was used [28–30]. The resulting energy resolution is $\approx 2 \text{ eV}$ at the Pt_{L3} edge (22.127 keV) and $\approx 1 \text{ eV}$ at the Ru_K edge (11.573 keV) [31]. As a consequence of the energy dispersion of the monochromator, a gradient over the height of the radiograms cannot be avoided. This gradient is about 2 eV mm^{-1} at the Pt_{L3} edge and approximately 6 eV mm^{-1} at the Ru_K edge, but can be easily corrected by taking several images at different energies around the investigated X-ray edges.

For image acquisition, a PCO4000 camera system with a total resolution of 4008×2672 pixels was applied. The spatial resolution of $2.1 \mu\text{m}$ results in a field of view of $8.6 \text{ mm} \times 4.2 \text{ mm}$. A $20 \mu\text{m}$ CdWO₄ scintillator and an exposure time of 10 s was used. The specimen was orientated in through-plane view [29].

3. Technique

3.1. X-ray absorption edge imaging

For typical NEXAFS or XANES measurements at a synchrotron X-ray source spot sizes of a few mm^2 are used to obtain a good signal-to-noise ratio even for fast in-situ measurements [32]. However such measurements can also be performed with high spatial

resolutions [28] when special X-ray optics are used that provide a very small focused beam of down to $5 \mu\text{m}$ size, and thus a spatial resolution of about the same size. When large areas have to be analyzed, the spot has to be scanned over the sample, which is very time consuming. Here we demonstrate another way for such measurements. This technique is based on standard X-ray transmission radiography in combination with a monochromator set-up that provides high energy resolutions. A series of radiograms are taken at different X-ray energies. Thus each pixel of a radiogram shows the transmission through the sample for a defined energy. These series are taken between energies from below up to energies above of the relevant X-ray edge. In this way, an X-ray near edge absorption (NEXAFS/XANES) spectrum is obtained for each depicted pixel of the radiogram series. The spatial resolution does not depend on the size of an X-ray focus, but only on the spatial resolution of the imaging set-up that can be much better than the typical focus provided by X-ray optics. For normalization purposes, a flat field image (radiogram without sample) at each energy has to be taken.

3.2. Element mapping

Because of electron excitations the transmission of a given element strongly decreases at its X-ray absorption edge, while the transmission of other elements remains almost constant. When a radiogram below and another one above the X-ray edge energy are taken, the transmission signal does only change for the specific element whose edge is between both energies. The change in the transmission of all other materials is almost negligible. The energies used for analysis at the Pt_{L3} und the Ru_K edge are shown in Table 1. For these energies, the differences of the transmission values are about two orders of magnitudes higher for the selected element than for the other ones.

When a radiogram taken above the edge is divided by a radiogram taken below the edge, all materials but that one where the absorption edge is crossed increases due to the increase in the X-ray energy. Within regions with large amounts of the selected element the division of the radiograms delivers values clearly lower than 1.

Because of the high energy resolution of the monochromator setup (see “Experimental setup”) used it is possible to select a very small energy difference between the two radiograms and thus to increase the sensitivity and accuracy for the investigated element distribution. Fig. 1 shows typical XAS curve taken of an aged (artificially aged for 1700 h, see Section 4. Sample preparation) and a new Pt–Ru-based fuel cell catalyst at the Pt_{L3} edge and the corresponding width of the energy spectrum at two measurement points.

The total thickness of the Ru layer can be calculated from the divided radiograms at the energies E_1 and E_2 as follows:

$$\frac{I_1}{I_0} = e^{-\mu_C(E_1)d_C - \mu_F(E_1)d_F - \mu_{Pt}(E_1)d_{Pt} - \mu_{Ru}(E_1)d_{Ru}},$$

$$\frac{I_2}{I_0} = e^{-\mu_C(E_2)d_C - \mu_F(E_2)d_F - \mu_{Pt}(E_2)d_{Pt} - \mu_{Ru}(E_2)d_{Ru}} \quad (1)$$

with $E_2 > E_1$.

Table 1

Table with transmissions through a layer of given thicknesses of the elements present in the fuel cell and the relative difference between pairs of energies.

Element	Energy/transmission value					
	11.56 keV	11.59 keV	Diff. (%)	22.07 keV	22.18 keV	Diff. (%)
Platinum (2 μm)	0.727	0.436	-40.3	0.780	0.783	+0.3
Ruthenium (2 μm)	0.856	0.857	+0.1	0.974	0.846	-13.2
Carbon (240 μm)	0.928	0.928	+0.1	0.984	0.984	0.0
Fluorine (240 μm)	0.999	0.999	0.0	0.999	0.999	0.0

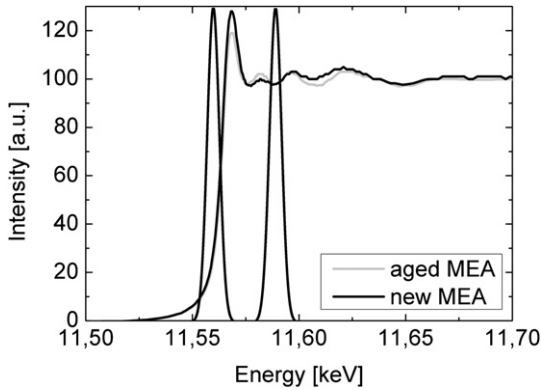


Fig. 1. Sketch of applied energies for element-sensitive mapping at the Pt_{L3} edge. The energy resolution is sufficient for the measuring proposes.

where $\mu_C(E_1)$ and $\mu_C(E_2)$, $\mu_F(E_1)$ and $\mu_F(E_2)$, $\mu_{Pt}(E_1)$ and $\mu_{Pt}(E_2)$, $\mu_{Ru}(E_1)$ and $\mu_{Ru}(E_2)$ are the attenuation coefficients of carbon, fluorine, platinum and ruthenium at the energies E_1 and E_2 . The thicknesses are expressed by d_C , d_F , d_{Pt} and d_{Ru} . The measured intensities are I_1 and I_2 and I_0 is the intensity of the flat field image. The ratio of the radiogram above through the radiogram below the Ru_K edge is

$$\frac{I_2}{I_0} = \frac{e^{-\mu_C(E_2)d_C - \mu_F(E_2)d_F - \mu_{Pt}(E_2)d_{Pt} - \mu_{Ru}(E_2)d_{Ru}}}{e^{-\mu_C(E_1)d_C - \mu_F(E_1)d_F - \mu_{Pt}(E_1)d_{Pt} - \mu_{Ru}(E_1)d_{Ru}}}. \quad (2)$$

For $E_1 \approx E_2$ the attenuation coefficients for all elements except Ru are approximately equal:

$$\mu_C(E_1) \approx \mu_C(E_2), \mu_F(E_1) \approx \mu_F(E_2), \mu_{Pt}(E_1) \approx \mu_{Pt}(E_2). \quad (3)$$

One obtains

$$d_{Ru} = \frac{\ln\left(\frac{I_2}{I_1}\right)}{\mu_{Ru}(E_1) - \mu_{Ru}(E_2)}. \quad (4)$$

Using Equation (4) the total Ru thickness can be calculated. Therewith the thickness of an element can be revealed by the transmittance only. A similar calculation is also used for platinum. Comparable calculations were done by Bigler et al. using photographic plates [33].

The calculated thickness can be calculated using Equation (5), where m_l is the loading of Ru (as specified by the manufacturer), A the normalized surface (1 cm^2) and ρ the mass density of Ru. Therewith, one achieves $d_{Ru} = 569 \text{ nm}$ (caused by a measured beam attenuation of $\approx 4.6\%$ in this case) and $d_{Pt} = 1534 \text{ nm}$. The material is assumed to be distributed homogeneously for unused samples.

$$d_{Ru} = \frac{m_l}{A \cdot \rho}. \quad (5)$$

4. Sample preparation

For the radiographic measurements, a MEA with an active area of 17.64 cm^2 was chosen. Carbon cloth (Ballard) was used as substrate for the electrodes. The texture of this woven material is shown in Fig. 2.

Both the catalyst layer and the microporous layer were prepared by knife-coating onto the carbon cloth. In a first step, a microporous layer containing 60 wt.% carbon (Cabot) and 40 wt.%

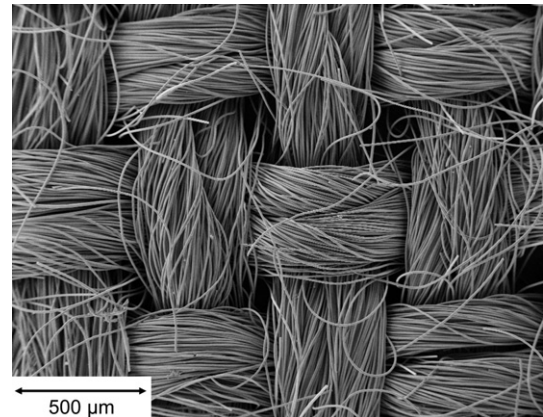


Fig. 2. Scanning electron micrograph of the carbon cloth used for the electrode preparation.

polytetrafluoroethylene (PTFE) was prepared on the carbon cloth. Then, the complete gas diffusion electrodes (GDEs) were obtained by preparing either anode or cathode catalyst layers on top of the micro layers. The anode catalyst layer contained Johnson Matthey carbon black supported platinum/ruthenium catalyst (HiSpec12100) and the cathode catalyst layer was prepared with Johnson Matthey carbon black supported platinum catalyst (HiSpec9100). A noble metal catalyst loading of about 2 mg cm^{-2} was used for both electrodes. Finally, the electrodes were hot-pressed (130°C , 0.5 kN cm^{-2}) on both sides of a Nafion-115 polymer membrane (Dupont).

The MEA was 'artificially' aged, i.e. subjected to an accelerated aging procedure of methanol depletion. The methanol depletion process was performed as follows: First of all, the MEA was operated with 1 M methanol solution and air (stoichiometry of $\lambda_{\text{methanol}} = \lambda_{\text{air}} = 4$) at a temperature of 70°C and a current density of 250 mA cm^{-2} . In the next step, the methanol supply was stopped for 400 s, resulting in fuel depletion at the anode. Instead of methanol oxidation, water oxidation accompanied by generation of oxygen and protons took place. Simultaneously, the anode potential increased up to more than 1.2 V/SHE (standard hydrogen electrode) and the cell voltage decreased to values far below zero ('cell reversal'). The high anode potential gave rise to corrosion of the anode catalyst, especially of ruthenium, as well as corrosion of the carbon black support. After 400 s, a cell voltage of -2 V was achieved and the methanol feed was immediately started again. After this accelerated aging test, the MEA was irreversibly damaged due to the partially dissolution of the catalyst support, which is oxidized to carbon dioxide at anode side instead of the lacking methanol.

4.1. Explanation of the sample aging procedure

The degradation protocol is an accelerated aging procedure representing a complete or local depletion of methanol supply of (a) stack cell(s) during a long term DMFC operation. As pointed out by Valdez et al. [34], the liquid manifold of a DMFC stack filled by methanol solution saturated with carbon dioxide provides a path for shunt currents and in combination with methanol depletion will lead to an oxidation and corrosion of the catalyst by electrolysis. In single cell experiments, this electrolysis process in combination with local methanol depletion can well be simulated by applying a current and stopping the methanol flow. The suitability of our aging protocol was also evidenced by the analysis of stack cells in 2005 which were operated in one of our DMFC systems driving a 4-wheel scooter [35]: The Ru corrosion in the anodes and

the deposition of Ru in the cathode was similar to that of the aged single cells exposed to methanol depletion.

5. Results

Two sets of radiographic measurements at different energies around the $\text{Pt}_{\text{L}3}$ edge and the Ru_{K} edge were taken of the aged MEA. From each image set two radiograms were chosen as described above. The chosen energies were 11.56 keV and 11.59 keV for the $\text{Pt}_{\text{L}3}$ edge and 22.17 keV and 22.23 keV for the Ru_{K} edge, respectively.

The ratios of these images were calculated in order to reveal the Pt and the Ru distribution (see above). The results are shown in Fig. 3a and b ($\text{Pt}_{\text{L}3}$ edge) and Fig. 3c and d (Ru_{K} edge). Pt is almost homogeneously distributed over the sample with some larger local agglomerations (Fig. 3a). In contrast, the Ru distribution shows strong density variations (Fig. 3c and d). Furthermore the variations are strongly correlated to the flow field of the fuel cell, which has schematically been added to Fig. 3b and d. Note: The crack structure leaving small 'lands' within the functional layers (mainly the electrodes at both sides of the membrane), which can be observed in each picture originates from drying during MEA preparation. As there is Pt on both sides of the membrane the Pt distribution in Fig. 3a and b shows more cracks than the images of the Ru distribution.

6. Pt and Ru thickness quantification

For a detailed analysis we have quantified the Pt and Ru distributions in accordance with Equation (4). The result is shown in Fig. 4a. The averaged thickness values (Fig. 4a) show that the Ru thickness below the channel area is larger than below the rib area, with the assumption that there are no changes of transmission caused by other elements.

The local thicknesses of Pt and Ru vary strongly. The corresponding thickness distributions are shown in Fig. 5. A Gaussian fit to the curves reveals that the average Ru thickness is about 408 ± 20 nm underneath the ribs and 532 ± 20 nm underneath channels. The widths of the graphs (full width at half maximum) are about 454 nm and 486 nm.

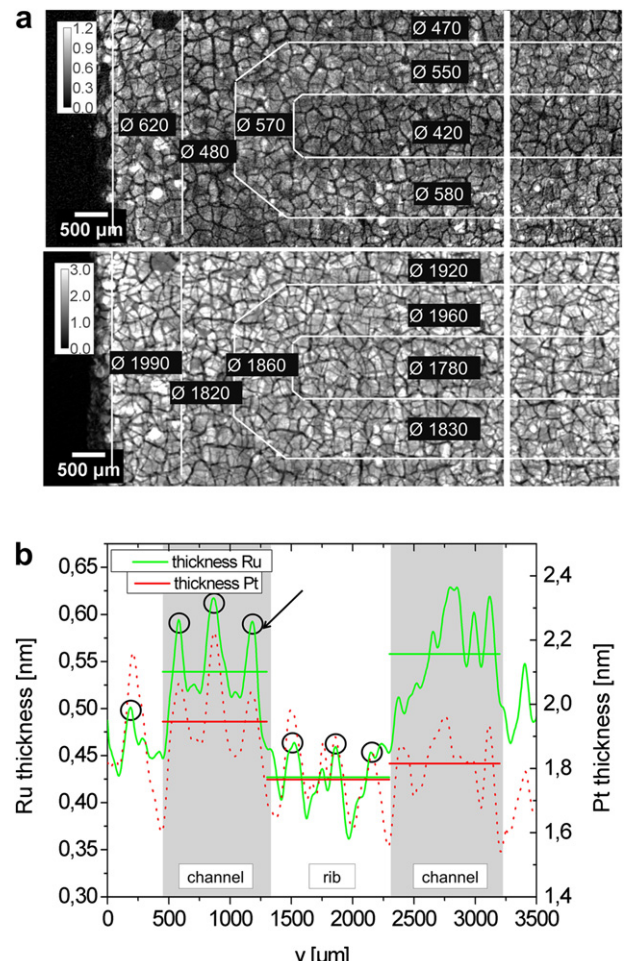


Fig. 4. a: Partially resolved Ru thickness (above) and Pt thickness (beneath) in gray values with averaged (marked by symbol 'Ø') thicknesses in nm beneath of the aged sample. Figure b shows thickness profiles along the white lines in Fig. 3b and d perpendicular to the former flow field course. Horizontal lines mark regions of constant thickness below ribs and channels.

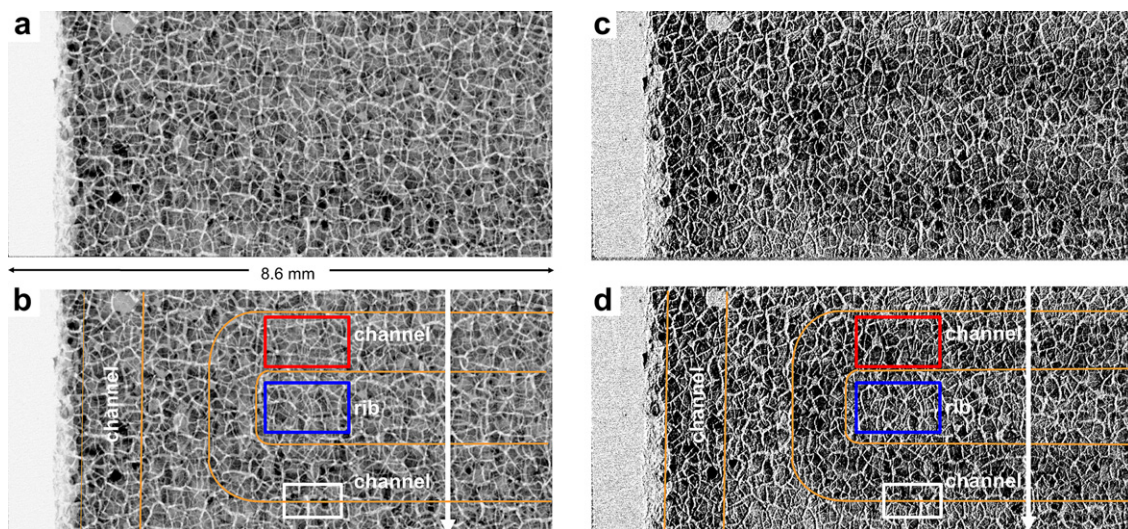


Fig. 3. Figures representing Pt sensitive measurements are shown in a and b; Ru sensitive measurements are shown in c and d. a and c: radiogram taken above the edge divided by the radiogram taken below the edge of the aged MEA. The former flow field characteristics are schematically overlaid in b and d while the white lines represent the path of the plot in Fig. 4b.

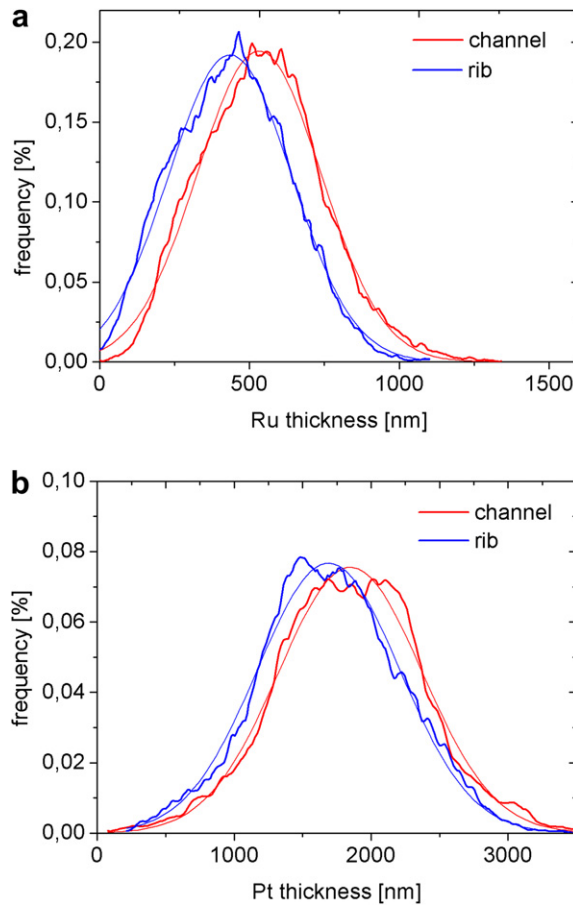


Fig. 5. Frequency of a) Ru thickness and b) Pt thickness of the aged sample. Thicknesses within intervals of 0.16 nm for the Pt distribution and 0.49 nm for the Ru distribution were summed up for each value of the distributions.

Taking the initial RuPt loading into account an average thickness of 569 nm Ru at the anode catalyst in the fresh material can be calculated. A decrease in Ru thickness (i.e. the Ru density) of around 6% (down to 532 ± 20 nm Ru) for the area under the channel and of around 28% (408 ± 20 nm Ru) for the area under the rib were found (see Fig. 4), i.e. approximately one third of the total Ru amount ($(569 \text{ nm} - 408 \text{ nm})/569 \text{ nm} = 28.3\%$) had been “washed out” of this area during cell operation. Accordingly, the difference in the average thicknesses (values in Fig. 4a) between the channels and the ribs is about 124 ± 20 nm.

On the other hand, the average Pt thickness was found to be about 1689 ± 60 nm underneath the ribs and 1848 ± 60 nm underneath channels in the aged sample, i.e. not only the Ru but also the Pt thickness is slightly reduced under the rib area, although the effect is much smaller compared to Ru. The width of the Pt thickness distribution graphs is about 1223 nm. As a total Pt thickness of 1632 nm was calculated (basing on manufacture information), a non-uniform distribution of Pt cannot be excluded, as differences of the loading over the active area of only a few tens ng cm^{-2} can induce the measured deviation. Actually these differences are expected within one batch. Also, the calculated Pt thicknesses for a fresh sample are equal to the measured thicknesses in the aged sample within the accuracy of the measurement.

Fig. 4b depicts the plot along the white lines in Fig. 3b and d. The arrow marks a Ru agglomeration in the channel along the interface to the rib underneath. Furthermore a periodic pattern of the Ru distribution is visible, accented by black circles in Fig. 4b. This

structure has a periodicity of about 500 μm and is correlated to the structure of the carbon cloth, which has a similar periodicity (see Fig. 2). Previous studies had already shown a redistribution of Ru due to aging processes that caused a similar structure [26]. It has been assumed that the increased transport of CO_2 gases/methanol solution through the voids in the GDL material (Fig. 2) causes a redistribution of Ru, i.e. the washed out Ru has been transported along these voids and therefore the Ru distribution shows the same periodic structure as the GDL material.

The dotted curve depicts the Pt distribution which is obviously also slightly impacted by the flow field geometry and even more by the periodic structure of the GDL, i.e. the catalyst layers (see Fig. 4b).

Not only variations in the local amount of Ru were found but also the chemical structure was found to have altered. Fig. 6a shows two XAS spectra: One taken from the area below the flow field channel (see red frame (in web version) in Fig. 3d) and the other taken from an area that was located below the rib of the flow field structure (see blue frame (in web version) in Fig. 3d). Both spectra show a clear difference in the intensity at the edge that hints toward a change in the chemical state.

At the same locations spectra taken at the $\text{Pt}_{\text{L}3}$ edge were also investigated (see Fig. 6b). Here a change in the edge heights is shown. Although the Pt distribution may not be as affected as that of Ru by aging, the chemical state was visibly changed.

At last we analyzed the XAS spectra on a smaller scale in areas with varying Pt (Fig. 7b) and Ru (Fig. 7d) thicknesses. For this purpose we chose three different locations with large (P1), medium (P2) and small (P3) Pt and Ru thicknesses. We found variations in the peak height of the corresponding XAS spectrum as shown in the Fig. 7b and d. The peak heights at the Pt (Ru) edge both increase with decreasing Pt (Ru) thicknesses.

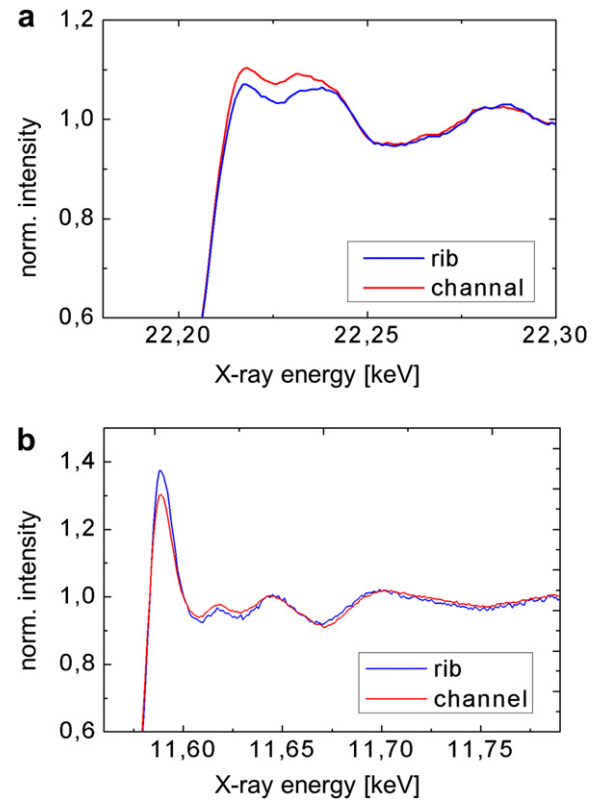


Fig. 6. XAS curves, taken from areas under the rib and under the channel for the Ru_K edge (a) and the $\text{Pt}_{\text{L}3}$ edge (b) of the aged sample. For measuring areas, see Fig. 3b and d.

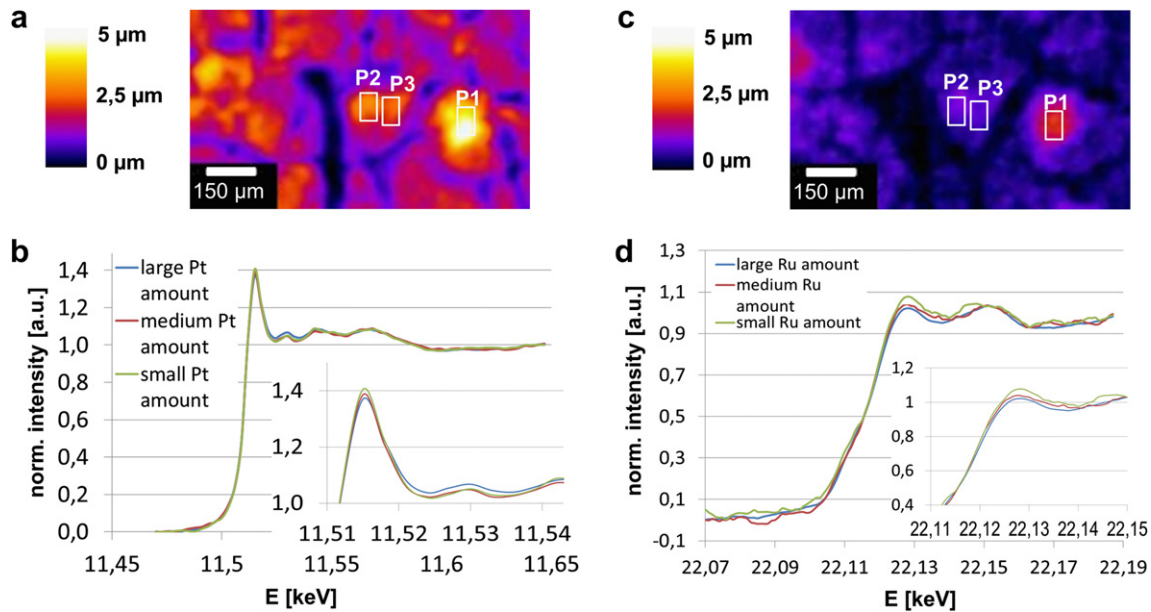


Fig. 7. a) Spatially resolved Pt thickness and c) Ru thickness encodes as gray values. XAS curves of regions with a large Pt amount (P1), medium Pt amount (P2) and less Pt amount (P3) b) at the $\text{Pt}_{\text{L}3}$ edge and d) at the Ru_{K} edge with enhanced insets of the near edge structure.

7. Discussion

Fig. 1 shows the relation between the energy width and the XAS curve profile. There is no overlap between both energy spectra – above and below the absorption edge. The measured transmittances can be dedicated to a much defined energy which enhances the accuracy of the theoretical calculations as the calculations are limited to exact energy values. Because of the use of high monochromatic X-rays, the X-ray energies are very clearly defined and therefore also the attenuation coefficients that are needed to quantify the Pt and Ru contents. It was also possible to take two X-ray energies very close to the X-ray edges. This is schematically shown in Fig. 1. Past studies (e.g. Ref. [26]) have used an X-ray energy spectrum width that was about 100 times broader than that shown in Fig. 1. In this case quantification cannot reach the high accuracy that we achieved with our high energy resolution. This is an important point since Equation (4) is only valid when the width of the energy peak is small enough. This allows for very sensitive measurements in future experiments where small changes in the amount of the catalysts can be observed with a spatial resolution of a few micrometers.

Haubold et al. [36] have shown a significant correlation between XAS peak height and the oxidation state of platinum. For PtO_2 the height of the X-ray absorption edge is much higher than the peak of non-oxidized Pt. Therefore, agglomerations with an overall lower Pt content (Fig. 7a) seem to contain more oxidized platinum, which could be explained by the relatively larger surface compared to that of the larger Pt agglomerations. Concerning the Ru_{K} edge, Aberdam et al. [37] demonstrated an increased peak height for oxidized Ru, as well. Following the assumption above, the impact of the oxidized Ru is also stronger in smaller Ru agglomerations.

More Pt and Ru can be found below the former flow field channels than under the ribs (Fig. 5a and b). Anyway the effect is much more pronounced for ruthenium. Since Ru is used to provide the bi-functional mechanisms and slightly modifies the interatomic distance of adjacent Pt atoms and therewith protect Pt from oxidation, the decreased total amount of Ru might be

a reason for the stronger Pt oxidation underneath the ribs (Fig. 6b) [38–44].

Previous studies have shown that CO_2 bubble formation and the paths of transport strongly depend on the GDL structure and the characteristics of the flow fields [45]. The increased Ru and Pt amounts below the channels could be explained by the entrainment of catalyst particles by carbon dioxide transport processes through the GDL toward the flow field. This can also explain the 500 μm periodicity of the found structure.

By using spatially resolved impedance spectroscopy, Schneider et al. have demonstrated limited mass transports underneath the ribs [46,47]. The lower peak in the XAS curve of Ru taken from underneath the rib can be attributed to less oxidized Ru due to oxygen depletion underneath the ribs [48,49].

8. Conclusion

We presented a powerful radiographic imaging technique based on high energy-resolution absorption edge measurements with synchrotron X-ray radiation. The thickness of a selected element and its distribution can be measured with a spatial resolution of a few micrometers and high quantification accuracy. Our measurement technique is non-destructive and non-invasive. It can be applied to in-situ/in-operando measurements and – in comparison to the novel approach of XAS imaging with focusing optics – no scanning is necessary and a high intense spot that might affect the material can be avoided. We investigated the Ru and Pt distribution of an artificially aged MEA of a direct methanol fuel cell. As one result, a strong influence of the former flow field characteristics on the catalyst distribution of the aged MEA was found. It is found that CO_2 , water and methanol transport paths have a great impact on the catalyst distribution. Furthermore, spatially resolved chemical information about oxidation states could be revealed.

The applied differential synchrotron X-ray absorption edge radiography technique is not limited to the study of aging of Pt and Ru, but can be used for various other future investigations on fuel cells and battery materials. In future in-situ measurements on

operating fuel cells or batteries might be interesting. Furthermore the technique can be extended to 3D investigations.

Acknowledgment

Funding of the project RuN-PEM (grant number: 03SF0324) by the Federal Ministry of Education and Research (BMBF) is gratefully acknowledged. The authors also like to thank Dr. H. Echlser from Forschungszentrum Jülich, IEK-3 for taking the micrograph.

References

- [1] A. Schröder, K. Wippermann, J. Mergel, W. Lehnert, D. Stolten, T. Sanders, T. Baumhöfer, D.U. Sauer, I. Manke, N. Kardjilov, A. Hilger, J. Schloesser, J. Banhart, C. Hartnig, *Electrochemistry Communications* 11 (2009) 1606–1609.
- [2] A. Schröder, K. Wippermann, W. Lehnert, D. Stolten, T. Sanders, T. Baumhöfer, N. Kardjilov, A. Hilger, J. Banhart, I. Manke, *Journal of Power Sources* 195 (2010) 4765–4771.
- [3] A. Schröder, K. Wippermann, G. Zehl, D. Stolten, *Electrochemistry Communications* 12 (2010) 1318–1321.
- [4] A. Bazylak, D. Sinton, N. Djilali, *Journal of Power Sources* 176 (2008) 240.
- [5] P.K. Sinha, C.-Y. Wang, *Electrochimica Acta* 52 (2007) 7936.
- [6] P. Zhou, C.W. Wu, *Journal of Power Sources* 195 (2010) 1408.
- [7] S. Listter, D. Sinton, N. Djilali, *Journal of Power Sources* 154 (2006) 95.
- [8] J.J. Kowal, A. Turhan, K. Heller, J. Brenizer, M.M. Mench, *Journal of the Electrochemical Society* 153 (2006) A1971.
- [9] P. Piela, C. Eickes, E. Broska, F. Garzon, P. Zelenay, *Journal of the Electrochemical Society* 151 (2004) A2053.
- [10] J.T. Wang, S. Wasmus, R.F. Savinell, *Journal of the Electrochemical Society* 143 (1996) 1233.
- [11] Z. Qi, A. Kaufman, *Journal of Power Sources* 110 (2002) 177.
- [12] H.A. Gasteiger, N. Markovic, P.N. Ross, E.J. Cairns, *J. Phys. Chem.* 97 (1993) 12020.
- [13] D.R. Rolison, P.L. Hagans, K.E. Swider, J.W. Long, *Langmuir* 15 (1999) 774.
- [14] D. Dixon, K. Wippermann, J. Mergel, A. Schökel, S. Zils, C. Roth, *Journal of Power Sources* 196 (2011) 5538–5545.
- [15] T. Saida, W. Sugimoto, Y. Takasu, *Electrochimica Acta* 55 (2010) 857.
- [16] J. Banhart (Ed.), *Advanced Tomographic Methods in Materials Research and Engineering*, Oxford University Press, Oxford, UK, 2008.
- [17] I. Manke, H. Markötter, C. Tötzke, N. Kardjilov, R. Grothausmann, M. Dawson, S. Haas, D. Thomas, A. Hoell, C. Genzel, C. Hartnig, J. Banhart, *Advanced Engineering Materials* 13 (8) (2011) 712–729.
- [18] T. Sasabe, P. Deevanhxay, S. Tsushima, S. Hirai, *Electrochemistry Communications* 13 (2011) 638–641.
- [19] P.K. Sinha, P. Halleck, C.-Y. Wang, *Electrochemical and Solid-State Letters* 9 (2006) A344–A348.
- [20] J. Banhart, A. Borbely, K. Dzieciol, F. Garcia-Moreno, I. Manke, N. Kardjilov, A.R. Kaysser-Pyzalla, M. Strobl, W. Treimer, *International Journal of Materials Research* 101 (2010) 1069–1079.
- [21] R. Thiedmann, C. Hartnig, I. Manke, V. Schmidt, W. Lehnert, *Journal of the Electrochemical Society* 156 (11) (2009) 1339–1347.
- [22] P. Krüger, H. Markötter, J. Haufmann, M. Klages, T. Arlt, J. Banhart, C. Hartnig, I. Manke, J. Scholte, *Journal of Power Sources* 196 (2011) 5250–5255.
- [23] H. Markötter, I. Manke, P. Krüger, J. Haufmann, M. Klages, T. Arlt, H. Riesemeier, C. Hartnig, J. Scholte, J. Banhart, *Electrochemistry Communications* 13 (9) (2011) 1001–1004.
- [24] A.E. Russell, A. Rose, *Chemical Reviews* 104 (2004) 4613–4635.
- [25] R. Viswanathan, R. Liu, E.S. Smotkina, *Review of Scientific Instruments* 73 (2002) 5.
- [26] T. Arlt, I. Manke, K. Wippermann, C. Tötzke, H. Markötter, H. Riesemeier, J. Mergel, J. Banhart, *Electrochemistry Communications* 13 (2011) 826–829.
- [27] A. Rack, S. Zabler, B.R. Müller, H. Riesemeier, G. Weidemann, A. Lange, J. Goebels, M. Hentschel, W. Görner, *Nuclear Instruments and Methods in Physics Research Section A: Accelerators, Spectrometers, Detectors and Associated Equipment* 586 (2008) 327–344.
- [28] W. Görner, M.P. Hentschel, B.R. Müller, H. Riesemeier, M. Krumrey, G. Ulm, W. Dieter, U. Klein, R. Frahm, *Nuclear Instruments and Methods in Physics Research Section A: Accelerators, Spectrometers, Detectors and Associated Equipment* 467–468 (2001) 703–706.
- [29] I. Manke, C. Hartnig, M. Grünerbel, W. Lehnert, N. Kardjilov, A. Haibel, A. Hilger, J. Banhart, H. Riesemeier, *Applied Physics Letters* 90 (2007) 174105.
- [30] I. Manke, C. Hartnig, N. Kardjilov, H. Riesemeier, J. Goebels, R. Kuhn, P. Krüger, J. Banhart, *Fuel Cells* 10 (2010) 26–34.
- [31] <http://physics.nist.gov/PhysRefData/XrayTrans/Html/search.html> (accessed 09.03.11).
- [32] C. Roth, D.E. Ramaker, in: C. Vayenas (Ed.), *Modern Aspects of Electrochemistry*, vol. 49, 2010, pp. 159–201 (chapter 3).
- [33] E. Bigler, F. Polack, S. Lowenthal, *Optics Communications* 41 (1981) 1.
- [34] T.I. Valdez, S. Firdosy, B.E. Koel, S.R. Narayanan, *ECS Transactions* 1 (6) (2006) 293–303.
- [35] J. Mergel, K. Wippermann, *Galvanotechnik* 3 (2009) 535–540.
- [36] H.-G. Haubold, X.H. Wang, H. Jungbluth, G. Goerigk, W. Schilling, *Journal of Molecular Structure* 383 (1996) 283–289.
- [37] D. Aberdam, R. Durand, R. Faure, F. Gloaguen, J.L. Hazemann, E. Herrero, A. Kabbabi, O. Ulrich, *Journal of Electroanalytical Chemistry* 398 (1995) 43–47.
- [38] M.P. Hogarth, G.A. Hards, *Platinum Metals Review* 40 (1996) 150.
- [39] A. Hamnett, *Catalysis Today* 38 (1997) 445.
- [40] J.B. Goodenough, A. Hamnett, B.J. Kennedy, R. Manoharan, S.A. Weeks, *Journal of Electroanalytical Chemistry* 240 (1988) 133.
- [41] D. Chu, S. Gilman, *Journal of the Electrochemical Society* 143 (1996) 1685.
- [42] V. Radmilovic, H.A. Gasteiger, P.N. Ross Jr., *Journal of Catalysis* 154 (1995) 98.
- [43] H.A. Gasteiger, P.N. Ross Jr., E. Cairns, *Surface Science* 293 (1993) 67.
- [44] M. Watanabe, S. Motoo, *Journal of Electroanalytical Chemistry* 60 (1975) 267.
- [45] C. Hartnig, I. Manke, J. Schloesser, P. Krüger, R. Kuhn, H. Riesemeier, K. Wippermann, J. Banhart, *Electrochemistry Communications* 11 (2009) 1559–1562.
- [46] I.A. Schneider, D. Kramer, A. Wokaun, G.G. Scherer, *Journal of the Electrochemical Society* 154 (2007) B770.
- [47] I.A. Schneider, M.H. Bayer, A. Wokaun, G.G. Scherer, *ECS Transactions* 25 (1) (2009) 937.
- [48] A.A. Kulikovsky, *Electrochemistry Communications* 2 (2001) 460–466.
- [49] I.A. Schneider, M.H. Bayer, S. von Dahlen, *Journal of the Electrochemical Society* 158 (3) (2011) B343–B348.